Superconducting properties of in-plane W-C nanowires grown by He+ Focused Ion Beam Induced Deposition

Orús, P.; Córdoba, R.; Hlawacek, G.; de Teresa, J. M.;

Originally published:

November 2020

Nanotechnology 32(2020)8, 085301

DOI: https://doi.org/10.1088/1361-6528/abc91c

Superconducting properties of in-plane W-C nanowires grown by He^+ Focused Ion Beam Induced Deposition

To cite this article before publication: Pablo Orús *et al* 2020 *Nanotechnology* in press https://doi.org/10.1088/1361-6528/abc91c

IOP Publishing Nanotechnology
Nanotechnology **XX** (XXXX) XXXXXX https://doi.org/XXXX/XXXX

Superconducting properties of in-plane W-C nanowires grown by He^+ Focused Ion Beam Induced Deposition

Pablo Orús[1,2,5,*], Rosa Córdoba[3,*], Gregor Hlawacek[4] and José María De Teresa[1,2,5,*]

[1] Instituto de Nanociencia y Materiales de Aragón (INMA), CSIC-Universidad de Zaragoza, 50009 Zaragoza, Spain
[2] Departamento de Física de la Materia Condensada, Facultad de Ciencias, Universidad de Zaragoza, 50009 Zaragoza, Spain
[3] Instituto de Ciencia Molecular, Universitat de València, Paterna, 46980 València, Spain
[4] Institute for Ion Beam Physics and Materials Research, Helmholz-Zentrum Dresden-Rossendorf, 01328 Dresden, Germany
[5] Laboratorio de Microscopías Avanzadas (LMA), University of Zaragoza, 50018 Zaragoza, Spain

E-mail: porus@unizar.es, rosa.cordoba@uv.es, deteresa@unizar.es

Received xxxxxx
Accepted for publication xxxxxx
Published xxxxxx

Abstract

Focused Ion Beam Induced Deposition (FIBID) is a nanopatterning technique that makes use of a focused beam of charged ions to decompose a gaseous precursor. So far, the flexible patterning capabilities of FIBID have been widely exploited in the fabrication of superconducting nanostructures, using the $W(CO)_6$ precursor mostly in combination with a focused beam of Ga^+ ions. Here, the fabrication and characterization of superconducting in-plane tungsten-carbon (W-C) nanostructures by He^+ FIBID of the $W(CO)_6$ precursor is reported. A virtually unattainable for Ga^+ FIBID patterning resolution of 10 nm has been achieved. When the nanowires are patterned with widths of 20 nm and above, the deposited material is superconducting below 3.5 – 4 K. In addition, 60 and 90 nm-wide nanostructures have been found to sustain long-range controlled non-local superconducting vortex transfer along 3 μm. Overall, these findings strengthen the capabilities of He^+ FIBID of W-C in the growth and patterning of in-plane superconducting nanodevices.

Keywords: superconductivity, Helium Ion Microscopy, FIBID, nanowires, vortex dynamics, electrical transport properties

1. Introduction

Superconducting materials are an evergreen hot topic in both the applied and basic research fields. The non-dissipative regime is an appealing framework for the design of advanced devices such as single-photon detectors [1], quantum switches [2], and nano-resonators [3]; as well as for the investigation of intriguing physical phenomena like single-vortex quantum dynamics [4], charge imbalance [5], and Andreev reflection physics [6] at superconducting-normal interfaces.

Type-II superconductors are characterized by a *mixed state*, found below the critical temperature and bound by the upper and lower critical magnetic fields, on which the magnetic flux lines that would normally be expelled from the bulk (Meissner effect) pierce the material in an ordered, quantized form. In the mixed state, a lattice of superconducting Abrikosov or Pearl vortices forms [7] [8], each vortex being a locally non-

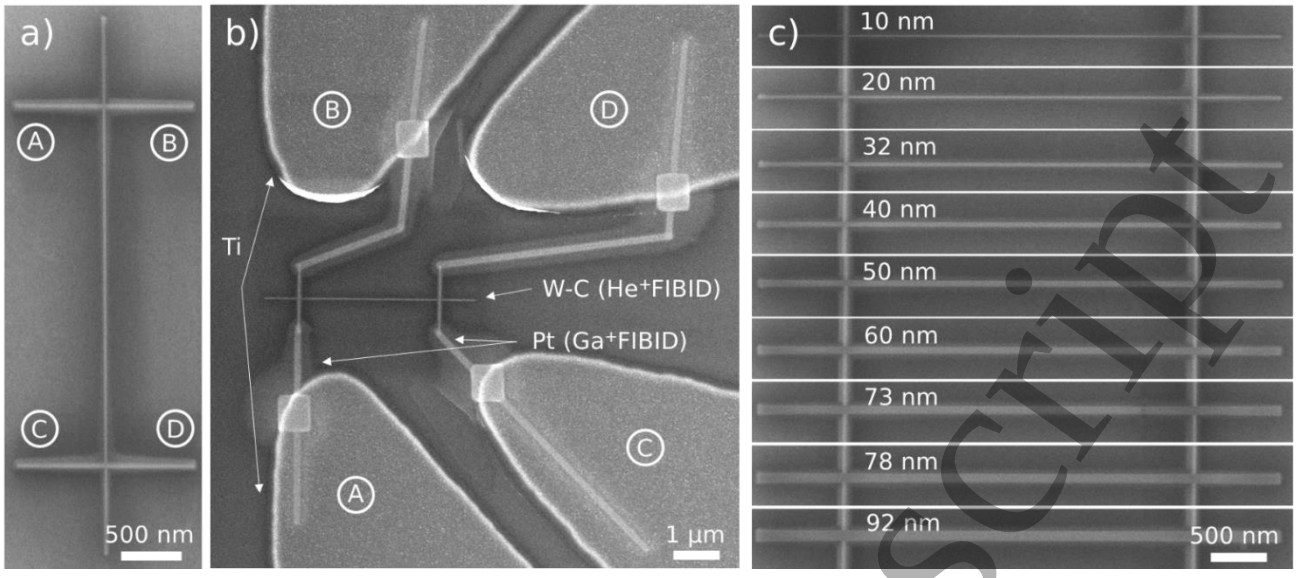

Figure 1. (a) SEM image of a representative 20 nm-wide NW, with the transversal leads labeled AB and CD. In a local measurement, the driving current flows from A to C and voltage is measured between B and D, while in a non-local measurement, current flows from A to B, and voltage is measured between C and D. **(b)** SEM image of a NW connected to the Ti pads by Pt contacts grown by Ga^+ FIBID. **(c)** SEM images showing NWs of increasing nominal width from 10 up to 90 nm (in steps of 10 nm) grown with a dose of 0.7 nC/µm^2. The actual width is indicated for each NW (± 2 nm). SEM images for the batch grown with 2.0 nC/µm^2 are available in the Supplementary Information.

superconducting tubular region threaded by a single quantum of magnetic flux and screened by a circular supercurrent. Vortices move when a driving current is injected in the material, dissipating energy in their motion. As such, vortex motion is usually regarded as an unwanted side effect, and significant research effort has already been directed towards immobilizing the vortices to avoid the associated energy losses. [9]–[12] Due to their quantized nature, however, vortices exhibit the potential to be used as information carriers, and control of their motion is also an appealing field of study [13] [14].

One noteworthy approach to the fabrication of superconducting nanostructures is growth via Focused Ion Beam Induced Deposition (FIBID), in which a beam of charged ions is used to decompose a gaseous precursor adsorbed on the surface of a substrate [15]. This single-step nanofabrication approach provides with great flexibility and ease of use in the patterning of complex nanostructures, since the beam can be scanned at will to obtain the required pattern shape.

The tungsten-carbon material obtained by Ga^+ FIBID of the tungsten hexacarbonyl ($W(CO)_6$) presents superconducting properties [16] and its study is extensively reported [17]–[20]. Typical material parameters include a W atomic content of 40-50%, lack of crystallinity (or extremely short-ranged, in the form of nm-sized nanocrystallites), a critical temperature (T_c) between 4 and 5 K, and an upper critical magnetic field (B_{c2}) of 9.5 T. Investigation of the physics of the Abrikosov vortices has also been performed, with results including direct imaging of the vortex lattice [21] [22], ocurrence of vortex confinement in narrow NWs [23], and long-range controlled non-local vortex transport [24].

The usage of a beam of He^+ ions to perform FIBID of $W(CO)_6$ is a more novel and less thoroughly explored approach. Due to the lighter mass of helium ions, He^+ FIBID overcomes some of the drawbacks of conventional Ga^+ FIBID, improving the patterning resolution down to 10 nm, as well as reducing sample amorphization and metal implantation [25]. Recent reports of He^+ FIBID of W-C centered on the growth of complex 3D structures such as hollow nanopillars [26] and nanohelices [27] indicate a 50-70% atomic content of W, crystallinity compatible with a WC_{1-x} phase, and values for T_c and B_{c2} of 6-7 K and above 11.6 T, respectively.

In addition, recent work by Basset *et al.* [3] makes usage of He^+ FIBID to grow in-plane W-C NWs with diameters down to 35 nm as constituents of hybrid microwave resonators. Other than that, as of the present day reports on He^+ FIBID for growth of in-plane superconducting W-C are absent from the literature. Here, the growth of in-plane W-C NWs by He^+ FIBID and a characterization of their compositional, microstructural, and superconducting properties are reported.

2. Experimental details

The deposition of the samples was performed in a commercial Zeiss ORION NanoFab Helium Ion Microscope. The standard values for the acceleration voltage and ion beam current were set to 25-30 kV and 15 ± 1.5 pA respectively. Mainly two ion doses were assessed: 0.7 and 2.0 nC/µm^2. The dwell time was set for these doses to 1 and 10 µs, respectively.

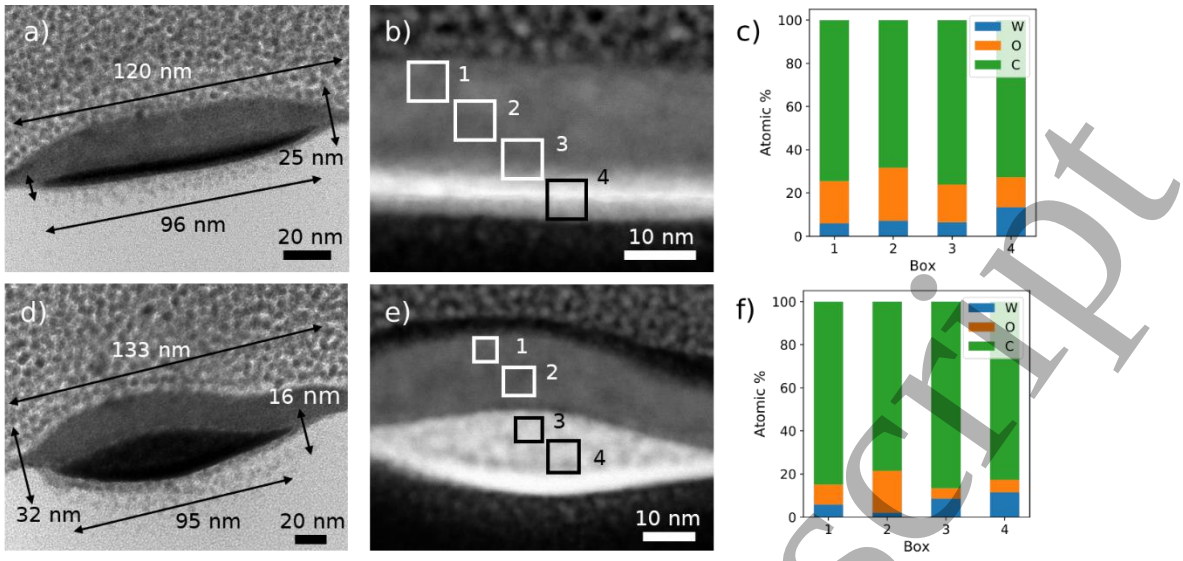

Figure 2. (a) HRTEM image of a cross-sectional view of a 90 nm-wide NW, grown with an ion dose of 0.7 nC/μm^2. The oxidized and metallic layers appear in grey and black tone, respectively. **(b)** HAADF image of the same NW. EDS was performed in each of the labeled boxes, yielding the composition distribution shown in **(c)**. **(d)-(e)-(f)** show the same TEM study performed for a 60 nm-wide NW grown with an ion dose of 2.0 nC/μm^2.

The pitch (separation between two adjacent irradiation spots) was set in both cases to 1 nm. The process chamber had a base pressure of 2-3·10^{-7} mbar, which was raised by the delivery of gaseous $W(CO)_6$ to 1·10^{-5} mbar during deposition. The nozzle used to inject the gas was positioned 50-100 μm away from the substrate in the vertical direction, and 200-250 μm away from the center in the substrate plane. The $W(CO)_6$ reservoir temperature was set to 55°C.

Silicon pieces with a 200 nm-thick thermally grown SiO_2 layer on top were used as a substrate. A series of Ti contacts had been previously grown on these substrates by means of optical lithography. After their deposition, the W-C nanostructures were joined to these contacts by growing Pt nano-contacts via Ga^+ FIBID in a commercial Thermo Fisher Helios 650 Dual Beam FIB/SEM instrument. Thereafter, the Ti pads were joined to electrical contacts in a sampleholder by ultrasonic bonding of Al wires.

The electrical characterization of the samples was carried in a commercial Quantum Design Physical Property Measurement System (PPMS) with a He^3 refrigerator insert.

All electrical measurements are taken as pairs of current-voltage points, while sequentially modifying the magnetic field and the temperature, when required. Depending on the configuration of the current and voltage electrodes, each measurement is referred to as *local* or *non-local*, both of which are described in their corresponding sections.

The microstructure and local composition studies by Transmission Electron Microscopy (TEM) were carried in FEI TITAN^3 and FEI Titan Low-Base instruments. The former was used to retrieve high resolution TEM images (HRTEM), and the latter was employed in Scanning TEM mode (STEM) to perform Energy-Dispersive X-Ray Spectroscopy (EDS) and High Angle Angular Dark Field (HAADF) imaging.

3. Results

3.1 Sample growth

The NWs were all grown with an ion beam current of 15 pA, and patterned with two transversal leads used to apply the driving current and measure voltage in a pseudo-four-probe configuration (Fig. 1 and Fig. S1). Two ion doses were assessed: 0.7 and 2.0 nC/μm^2 (calculated by estimating the area from the ion beam spot size, and deducting the charge from the ion beam current and the irradiation time). Different NWs were grown varying the width of the path between the two leads (henceforth "the long axis of the NW") from 10 to 90 nm. Both transversal leads are separated 3 μm one from the other, and their ends are each 750 nm away from the long axis of the NW, to ensure that the path is not contaminated or damaged during the Ga^+ FIBID deposition of the auxiliary Pt contacts.

3.2 Composition and microstructure

TEM compositional and microstructural studies were performed on two different NWs deposited with ion doses of 0.7 and 2.0 nC/μm^2, and both grown with an ion beam current of 15 pA. STEM-HAADF/EDS analyses reveal the presence of two different layers within the deposit, the one in the top presenting a higher atomic percentage of oxygen (Fig. 2 and Figs. S2, S3 and S4) and a lower tungsten content than the one in the bottom.

The thickness of the metallic part is around 5 and 15 nm for the NWs grown with doses of 0.7 and 2.0 nC/μm^2, respectively. An atomic W content up to 10-15% is found (samples with higher amount of W are reported in the

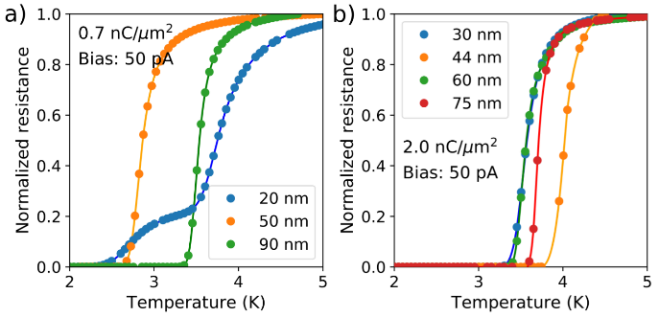

Supplementary Information). Concerning the microstructure,

Figure 3. Superconducting transitions of samples of variable width grown with ion doses of **(a)** 0.7 nC/μm² and **(b)** 2.0 nC/μm². In both cases, the driving current is set to 50 pA. For clarity, each resistance has been normalized to its corresponding value of R_{10K}. In increasing width order of the shown curves, R_{10K} equals **(a)** 46, 27, and 12 kΩ, and **(b)** 13, 11, 8, and 6 kΩ. Solid lines are a guide to the eye.

for both ion doses, structurated domains or crystallites, with size in the order of 5 nm, can be observed. They appear embedded in a predominantly amorphous matrix.

For the purposes of the present study, the oxidized top layer does not hinder the electrical characterization, since due to its insulating behavior, it does not contribute to the electrical conduction, with only the lower, metallic layer being probed. The lack of such a layer would represent an increase in the effective thickness value, yielding reduced values of total resistance, but it would not significantly alter the superconducting properties.

3.3 Local electrical characterization

The *local* measurement mode is comparable to a conventional four-probe measurement – a driving current flows through the long axis of the NW and the corresponding voltage is measured in-between (from A to C and from B to D in Fig. 1, respectively). In this disposition, the auxiliary Ga^+ FIBID Pt contacts do not contribute to the measured voltages. However, since both the current and voltage leads are placed on the same W-C transversal lead, a small contribution to ρ arises from dissipation in this small area, and as such, the retrieved values are slightly overestimated.

The samples display ohmic behavior at room temperature. The room-temperature resistivities, ρ_{300K}, are estimated by taking the average thickness of the non-oxidized part of the cross-sections, and considering the 3 μm-long path between the transversal contacts only. For the NWs with the dose of 0.7 nC/μm² ρ_{300K} ranges in the 120-200 μΩ·cm, while samples from the 2.0 nC/μm² batch exhibit values in the 170-250 μΩ·cm range. The resistivity increases with decreasing temperature, with the ρ_{10K}/ρ_{300K} ratio being around 1.1 in both cases.

In all NWs with width of 20 nm or higher, a temperature-induced transition to the superconducting state is observed. NWs grown with a dose of 0.7 nC/μm² exhibit values of T_c in the 2.5-3.5 K range, while those grown with a dose of 2.0

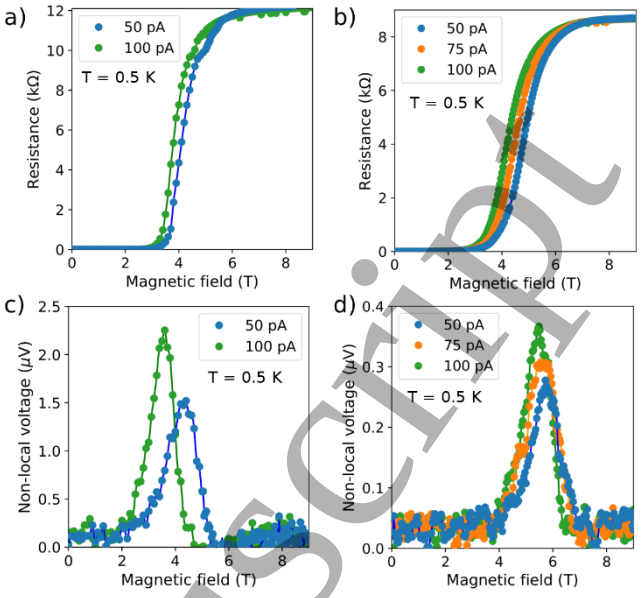

Figure 4. Local magneto-resistance curves of **(a)** a 90 nm-wide NW deposited with an ion dose of 0.7 nC/μm², and **(b)** a 60 nm-wide NW grown with an ion dose of 2.0 nC/μm². **(c)** and **(d)** show the non-local voltage dependence with field for the same NWs, respectively, where the magneto-resistance peaks associated to vortex transport via Lorentz force can be observed. Solid lines are a guide to the eye.

nC/μm² present them in the 3.7-4 K range (Fig. 3). Most of them show transition widths of around 0.5 K. The 10 nm-wide NWs (grown with a dose of 0.7 nC/μm²) do not display superconductivity within the measured range, down to 0.5 K.

According to the BCS theory, the measured values of critical temperature (at which $R(T_c)=0.5R_{10K}$) indicate a range of values for the superconducting gap at zero temperature, Δ_0, ($\Delta_0=1.76k_BT_c$, k_B being the Boltzmann constant) between 0.47 and 0.62 meV. The penetration depth of the material, λ, can be estimated from $\lambda=1.05\cdot10^{-3}(\rho_{300K}/T_C)^{1/2}$ (SI units) [28], yielding values in the 616-770 nm range for the batch grown with a dose of 0.7 nC/μm²; and in the 700-800 nm range for the batch grown with a dose of 2.0 nC/μm².

The value of B_{c2} (here defined as the value of the magnetic field B at which the resistance R exhibits a value such that $R(B_{c2})=0.9R_{10K}$), can be extrapolated to its nominal value at zero current and zero temperature from magneto-resistance dependences at different currents and temperatures (Fig 4 and Supplementary Information). The curves of the 60 nm-wide sample grown with a dose of 2.0 nC/μm² yield a zero temperature-extrapolated value of B_{c2} in the 8-9 T, and a subsequent coherence length, ξ, ($\xi^2=\Phi/2\pi B_{c2}$, Φ being the flux quantum) falls in the 6-6.4 nm range.

3.4 Non-local electrical characterization

Current-induced non-local vortex transport can be asessed by means of *non-local* voltage measurements. Contrary to the local approach, in non-local mode the driving current is made

flow through one of the leads, and the voltage is measured in the other, which is depleted of current (A to B, and C to D in Fig. 1a). [29]–[32]

NWs with a line width of 60 and 90 nm display finite values of non-local voltage (Fig. 4), indicating the occurrence of vortex motion along the 3 μm-long axis of the NW. The equivalent non-local resistances peak in the 5-20 Ω range, similarly to those reported in Ga^+ FIBID NWs [24].

4. Discussion

In-plane He^+ FIBID of W-C has been shown to yield a material with superconducting properties comparable to those obtained by Ga^+ FIBID, with the added values of enhanced lateral patterning resolution and reduced substrate amorphization and metal implantation that one technique provides over the other. Superconducting behavior occurs above withds of 20 nm, and non-local long-range vortex transport has been observed in 60 and 90 nm-wide NWs.

4.1 Composition and microstructure

Since the decomposition of the precursor $W(CO)_6$ is not ideal nor complete, in addition to W, significant amounts of C and O are to be expected in the composition of the samples. As evidenced by the TEM study, all NWs present an oxygen-rich upper layer that extends over at least half of the thickness of the deposited material (up to a 80% of the material is oxidized in the most extreme cases). It is likely that this oxygen-rich layer appeared after exposure to ambient conditions during sample handling and transportation, and grew with time until the TEM experiments were carried out. The low metallic content present in the oxidized layer limits the conductivity of the nanostructure to the lower, non-oxidized layer. Thus, the growth of a protective cover (*e.g.*, a carbon layer) for these nanostructures should be considered in future research, as successfully implemented in core-shell cobalt NWs grown by Focused Electron Beam Induced Deposition [33].

The composition of the non-oxidized part strongly differs to that retrieved in 3D NWs grown by He^+ FIBID and on in-plane NWs grown by Ga^+ FIBID, on which the W atomic content is found to typically reach 70% and 50%, respectively. The samples are not either as crystalline as the 3D He^+ FIBID, nor they can be deemed as fully amorphous as most reports in the literature claim W-C Ga^+ FIBID to be.

The remarkable differences between the in-plane NWs and the 3D nanostructures prepared by He^+ FIBID arise from the fact that despite sharing the same growth technique, the deposited materials are significantly different in terms of composition and microstructure. Conventional in-plane deposition takes place as the FIB induces the emission of secondary electrons (SEs) from the substrate that dissociate the adsorbed precursor molecules. 3D deposition occurs as as a competition between deposition and milling (above and of the previously deposited material), with first-order SEs (induced by the primary beam) driving the vertical growth, and second-order SEs (induced by scattered ions) promoting lateral growth [34] [35]. Differences in the composition and microstructure of the in-plane and 3D deposits can be first attributed to changes in the SE yield between the two processes and, secondly, to differences in ion-irradiation-induced local heating effect [36] .

	Present study	*2D He^+ FIBID* [3]	*3D He^+ FIBID* [26] [27]	*Ga^+ FIBID* [16], [20] [23]
W atomic content	20 – 30%	-	– 72%	50 – 70%
Crystallinity	Crystallites	-	WC_{1-x}	Amorphous/ Crystallites
ρ_N (μΩ·cm)	110-240	80-260	398-464	200-330
T_c (K)	2.5 – 4	5 – 6 K	6.2 – 7.1	4.2-5.1
B_{c2} (T)	8	>5	12.1-15.3	9.5
J_c (MA/cm^2)	0.12-0.46	0.25-0.86	0.09-0.23	0.01-0.1
ξ (nm)	6.4	6.7-7.6	4.64-5.22	6.25
λ (nm)	616-812	400- 674	603 – 902	850

Table 1. Structural properties and superconducting parameters of three different approaches used to grow superconducting W-C NWs via FIBID (when not directly specified by the authors, values have been estimated from geometrical and superconducting parameters).

When comparing the present samples to in-plane Ga^+ FIBID NWs, care must also be taken since implantation of Ga^+ and sample amorphization are two unavoidable features of this process, which also significantly modify the compositional and microstructural nature of the deposits.

4.2 Superconducting properties

Concerning the study of the local resistance, the superconducting parameters retrieved from this study are closer to that of in-plane Ga^+ FIBID W-C than to those of 3D He^+ FIBID W-C (Table 1). Thus, in-plane He^+ FIBID W-C NWs are also suitable for most of the purposes their Ga^+ counterparts would be, with the enhanced resolution achievable by the usage of these ion species as an added value.

The specific value of T_c varies between samples of different width lacking a clear trend, from where it can be assumed that width does not play a signficant role on its value, but rather the (small, but mostly unavoidable) compositional and microstructural differences between samples are responsible for it. In addition, the broadening of the superconducting transition in narrow nanostructures can also be attributed to the occurrence of phase slips, *i.e.*, local fluctuations of the superconducting parameter $\Psi=|\Psi|e^{i\varphi}$, where the phase φ "slips" by 2π. Phase slips locally drive finite regions in the NW to the normal state, resulting in average in a finite resistance of the NW below T_c. The driving force for phase slips is thermal in nature in the vicinity of T_c. Quantum phase slips are notably significant in narrow NWs (with widths below 10-20 nm) well below T_c, as supported by experimental evidence (similar in form to that reported here) on several

materials, including MoGe [37], Al [38], [39], Ti [40], and MoSi [41].

The broadening of the superconducting transition is particularly evident in the 20 nm-narrow NW, where it occurs through two wide (2 K) overlapping transitions. (Fig. 3a and Supplementary Information). This effect, which is also observed in the field-induced transition (Fig. S5), can be accounted for by the ocurrence of phase slips, and by the presence of local constrictions, either on the long axis of the NW or on the crossing points with the transversal leads. Since a width of 20 nm is close to the expected coherence length of the material (around 8 nm), phase-slip induced resistance is to be expected, and small constrictions can significantly alter the critical temperature of the material, with the whole nanostructure behaving as two NWs with different critical temperatures connected in series.

The non-local voltage peaks are a characteristic fingerprint of non-local vortex transport along the long axis of the NW. In this configuration, the driving current is expected to exert a Lorentz force $\boldsymbol{F_L}$ in vortices present on the lead, pushing them perpendicularly to both the magnetic field $\boldsymbol{B}$ and the driving current $\boldsymbol{J}$ ($\boldsymbol{F_L} \parallel \boldsymbol{J} \times \boldsymbol{B}$). Provided that the lattice is stiff enough, these vortices will in turn push neighboring ones, yielding net vortex motion along the long axis of the NW. The voltage they generate as they move is measured in the opposite lead.

For low values of applied magnetic field, the vortex density is low, with naturally ocurring pinning sites of the material keeping the vortices still against the Lorentz force exerted by the driving current. As a consequence, no non-local voltage is detected. As the magnetic field increases, so does the vortex density, eventually saturating the pinning sites and leading to the onset of vortex motion. The passage of vortices through the voltage lead of the nanostructure is detected in the form of a non-zero voltage value in the non-local magneto-resistance curves.

Further increasing the field results in more vortices passing through the lead, which in turn generate a larger voltage. This voltage-field positive trend is kept up to the critical value of the magnetic field, upon which the nanostructure transitates to the normal state (starting from the current lead, where the driving current is being injected). The transition results in a decrease of the non-local voltage, which eventually reaches zero when the whole nanostructure is in the normal state and no vortices are present. Since no current is flowing through the lead, the non-local voltage is at this point, zero once more.

In principle, efficient pressure transfer is achieved when the potential barriers for vortex motion located at the edges of the nanostructure are high enough to confine the vortex motion along the long axis of the NW, hampering transversal displacements. In much wider nanostructures (one order of magnitude and above), the pressure transfer is more inefficient due to a significant part of the total pressure being invested in transversally pushing the vortices, which do not reach the opposite end. They can also leave the NW through the potential wall. In these nanostructures, the absolute value of the non-local voltage is lower despite the number of hosted vortices being higher.

The efficient transfer of pressure is particularly favored when a single row of vortices is present on the nanostructure, and superconductivity reentrance in local mode can be detected as a signature [23]. While such a feature is not observed on the present NWs (due to the narrowest NWs not hosting any vortices at all and the wider NWs most likely hosting more than one row), the results are not in disagreement with this hypothesis, most likely indicating the existence of few vortex lines that still maintain the pressure transfer efficient. The difference in absolute values of non-local voltage between the 60 and 90 nm can be attributed to the wider channel hosting more vortex rows whilst keeping them confined enough for the pressure transfer to be effective. In any case, given that sample imperfections hamper the vortex motion, the presence of non-local vortex transport across 3 μm-long superconducting channels is a signature of the smoothness of the edges and thickness of the grown NWs by He^+ FIBID. On the other hand, when temperature approaches T_c, the magnitude of the non-local resistance peaks decreases and their position moves to lower magnetic fields (Fig. S6).

It is worth mentioning that reduced values of line width have the potential to restrict the appearance of superconducting vortices within the nanostructure. As noted by Stan *et al*. [42], superconducting vortices only "enter" a given nanostructure above a certain value of magnetic field, B_m, that is inversely proportional to the squared channel width W, $B_m \sim \Phi/W^2$. For the narrowest superconducting NWs (20 nm in width) this vortex entrance field equals ~5 T, which is above their critical field at the measured temperature. Therefore, these NWs cannot in principle host vortices at all in the experiment conditions. Wider NWs present lower values of B_m (0.6 and 0.2 T for widths of 60 and 90 nm, respectively), and thus vortices do enter the nanostructure within the experiment range. It should also be kept in mind that narrow NWs do not host an actual vortex Abrikosov "lattice", but rather fit one or two rows within. [23] The width limit can also be considered taking into account that to host vortices at a given temperature, a nanowire should at least have a width of 4.4ξ [43], roughly equalling 30 nm for ξ(0)=6.4 nm.

5. Conclusions

W-C nanostructures have been prepared by He^+ FIBID, achieving patterning resolutions of 10 nm, which would prove from challenging to virtually impossible to obtain using Ga^+ FIBID. Exhibiting a metallic content of around 20% and no ion implantation, nanostructures with line widths greater than 20 nm maintain the superconducting properties of their Ga^+ FIBID counterparts, with a critical temperature of around 3-4

K and an extrapolated zero-temperature critical magnetic field in the 8-9 T range. 60 and 90 nm-wide NWs sustain long-range vortex transport across 3 μm, yielding equivalent non-local resistances of up to 20 Ω solely caused by non-local vortex motion. He^+ FIBID of $W(CO)_6$ thus proves a promising technique for the deposition of in-plane extremely narrow superconducting functional nanostructures, such as rectifiers, vortex diodes, superconducting logic gates, single-photon detectors, nano-resonators, and QPS-based devices.

Acknowledgements

P. Orús acknowledges Aragón Government for funding. This work was supported by a STSM grant from COST Action CA16218. The HIM works were performed in the Ion Beam Center at the Helmholz-Zentrum Dresden-Rossendorf, the access to which and whose support is acknowledged. The project that gave rise to these results received the support of a fellowship from "la Caixa" Foundation (ID 100010434). The fellowship code is LCF/BQ/PR19/11700008. Authors acknowledge financial support from the Spanish Ministry of Economy and Competitiveness through Projects MAT2018-102627-T and MAT2017-82970-C2, from CSIC through project PIE202060E187, and from the Aragon Regional Government (Construyendo Europa desde Aragón) through Project E13_20R, with European Social Fund funding. The Ga^+ FIB, SEM, and TEM microscopy works have been conducted in the Laboratory for Advanced Microscopies (LMA), at the Institute of Nanoscience of Aragón (INA) – University of Zaragoza. Authors acknowledge the LMA-INA for offering access to their instruments and expertise. Authors acknowledge the use of Servicio General de Apoyo a la Investigación (SAI) – University of Zaragoza, particularly the Physical Measurements Service. TEM support provided by Dr. R. Hübner is acknowledged.

References

[1] C. M. Natarajan, M. G. Tanner, and R. H. Hadfield, "Superconducting nanowire single-photon detectors: physics and applications," *Supercond. Sci. Technol.*, vol. 25, no. 6, p. 063001, 2012, doi: 10.1088/0953-2048/25/6/063001.

[2] I. Chiorescu, Y. Nakamura, C. J. P. M. Harmans, and J. E. Mooij, "Coherent quantum dynamics of a superconducting flux qubit," *Science (80-.).*, vol. 299, no. 5614, pp. 1869–1871, 2003.

[3] J. Basset *et al.*, "High kinetic inductance microwave resonators made by He-Beam assisted deposition of tungsten nanowires," *Appl. Phys. Lett.*, vol. 114, no. 10, 2019, doi: 10.1063/1.5080925.

[4] A. Wallraff *et al.*, "Quantum dynamics of a single vortex," *Nature*, vol. 425, no. 6954, pp. 155–158, 2003, doi: 10.1038/nature01826.

[5] J. P. Veazey *et al.*, "Nonlocal current-voltage characteristics of gated superconducting sketched oxide nanostructures," *Epl*, vol. 103, no. 5, 2013, doi: 10.1209/0295-5075/103/57001.

[6] S. Russo, M. Kroug, T. M. Klapwijk, and A. F. Morpurgo, "Experimental observation of bias-dependent nonlocal Andreev reflection," *Phys. Rev. Lett.*, vol. 95, no. 2, 2005, doi: 10.1103/PhysRevLett.95.027002.

[7] E. H. Brandt, "The flux-line lattice in superconductors," *Reports Prog. Phys.*, vol. 58, no. 11, pp. 1465–1594, 1995, doi: 10.1088/0034-4885/58/11/003.

[8] J. Pearl, "Current distribution in superconducting films carrying quantized fluxoids," *Appl. Phys. Lett.*, vol. 5, no. 4, pp. 65–66, 1964, doi: 10.1063/1.1754056.

[9] J. I. Martín, M. Vélez, J. Nogués, and I. K. Schuller, "Flux pinning in a superconductor by an array of submicrometer magnetic dots," *Phys. Rev. Lett.*, vol. 79, no. 10, pp. 1929–1932, 1997, doi: 10.1103/PhysRevLett.79.1929.

[10] J. Gutiérrez *et al.*, "Strong isotropic flux pinning in solution-derived YBa 2Cu 3O7-x nanocomposite superconductor films," *Nat. Mater.*, vol. 6, no. 5, pp. 367–373, 2007, doi: 10.1038/nmat1893.

[11] M. Vélez *et al.*, "Superconducting vortex pinning with artificial magnetic nanostructures," *J. Magn. Magn. Mater.*, vol. 320, no. 21, pp. 2547–2562, 2008, doi: 10.1016/j.jmmm.2008.06.013.

[12] A. Palau, V. Rouco, R. F. Luccas, X. Obradors, and T. Puig, "Nanowall pinning for enhanced pinning force in YBCO films with nanofabricated structures," *Phys. C Supercond. its Appl.*, vol. 506, pp. 178–183, 2014, doi: 10.1016/j.physc.2014.06.011.

[13] J. E. Villegas *et al.*, "A superconducting reversible rectifier that controls the motion of magnetic flux quanta," *Science (80-.).*, vol. 302, no. 5648, pp. 1188–1191, 2003.

[14] T. Golod, A. Iovan, and V. M. Krasnov, "Single Abrikosov vortices as quantized information bits," *Nat. Commun.*, vol. 6, 2015, doi: 10.1038/ncomms9628.

[15] I. Utke, P. Hoffmann, and J. Melngailis, "Gas-assisted focused electron beam and ion beam processing and fabrication," *J. Vac. Sci. Technol. B Microelectron. Nanom. Struct.*, vol. 26, no. 4, p. 1197, 2008, doi: 10.1116/1.2955728.

[16] E. S. Sadki, S. Ooi, and K. Hirata, "Focused ion beam induced deposition of superconducting thin films," *Phys. C Supercond. its Appl.*, vol. 426–431, no. II, pp. 1547–1551, 2005, doi: 10.1016/j.physc.2005.02.151.

[17] I. J. Luxmoore *et al.*, "Low temperature electrical characterisation of tungsten nano-wires fabricated by electron and ion beam induced chemical vapour deposition," *Thin Solid Films*, vol. 515, no. 17, pp. 6791–6797, 2007, doi: 10.1016/j.tsf.2007.02.029.

[18] D. Spoddig *et al.*, "Transport properties and growth parameters of PdC and WC nanowires prepared in a dual-beam microscope," *Nanotechnology*, vol. 18, no. 49, p. 495202, 2007, doi: 10.1088/0957-4484/18/49/495202.

[19] W. Li, J. C. Fenton, and P. A. Warburton, "Focused-ion-beam direct-writing of ultra-thin superconducting tungsten composite films," in *IEEE Transactions on Applied Superconductivity*, 2009, vol. 19, no. 3, pp. 2819–2822, doi: 10.1109/TASC.2009.2019251.

[20] W. Li, J. C. Fenton, C. Gu, and P. A. Warburton, "Superconductivity of ultra-fine tungsten nanowires grown by focused-ion-beam direct-writing," *Microelectron. Eng.*, vol. 88, no. 8, pp. 2636–2638, 2011, doi: 10.1016/j.mee.2010.12.116.

[21] I. Guillamón *et al.*, "Direct observation of melting in a two-dimensional superconducting vortex lattice," *Nat.*

Phys., vol. 5, no. 9, pp. 651–655, 2009, doi: 10.1038/nphys1368.

[22] I. Guillamón *et al.*, "Direct Observation of Stress Accumulation and Relaxation in Small Bundles of Superconducting Vortices in Tungsten Thin Films," *Phys. Rev. Lett.*, vol. 106, no. 7, p. 77001, 2011, doi: 10.1103/PhysRevLett.106.077001.

[23] R. Córdoba *et al.*, "Magnetic field-induced dissipation-free state in superconducting nanostructures," *Nat. Commun.*, vol. 4, 2013, doi: 10.1038/ncomms2437.

[24] R. Córdoba *et al.*, "Long-range vortex transfer in superconducting nanowires," *Sci. Rep.*, vol. 9, no. 1, 2019, doi: 10.1038/s41598-019-48887-7.

[25] G. Hlawacek *et al.*, "Helium ion microscopy," *J. Vac. Sci. Technol. B, Nanotechnol. Microelectron. Mater. Process. Meas. Phenom.*, vol. 020801, 2015, doi: 10.1116/1.4863676.

[26] R. Córdoba, A. Ibarra, D. Mailly, and J. M. De Teresa, "Vertical Growth of Superconducting Crystalline Hollow Nanowires by He+Focused Ion Beam Induced Deposition," *Nano Lett.*, vol. 18, no. 2, pp. 1379–1386, 2018, doi: 10.1021/acs.nanolett.7b05103.

[27] R. Córdoba *et al.*, "Three-Dimensional Superconducting Nanohelices Grown by He+-Focused-Ion-Beam Direct Writing," *Nano Lett.*, vol. 19, no. 12, pp. 8597–8604, 2019, doi: 10.1021/acs.nanolett.9b03153.

[28] P. H. Kes and C. C. Tsuei, "Two-dimensional collective flux pinning, defects, and structural relaxation in amorphous superconducting films," *Phys. Rev. B*, vol. 28, no. 9, p. 5126, 1983.

[29] I. V. Grigorieva *et al.*, "Long-range nonlocal flow of vortices in narrow superconducting channels," *Phys. Rev. Lett.*, vol. 92, no. 23, p. 237001, 2004, doi: 10.1103/PhysRevLett.92.237001.

[30] A. Helzel *et al.*, "Nonlocal vortex motion in mesoscopic amorphous Nb0.7 Ge0.3 structures," *Phys. Rev. B - Condens. Matter Mater. Phys.*, vol. 74, no. 22, 2006, doi: 10.1103/PhysRevB.74.220510.

[31] F. Otto, A. Bilušić, D. Babić, D. Y. Vodolazov, C. Sürgers, and C. Strunk, "Nonlocal versus local vortex dynamics in the transversal flux transformer effect," *Phys. Rev. B - Condens. Matter Mater. Phys.*, vol. 81, no. 17, 2010, doi: 10.1103/PhysRevB.81.174521.

[32] F. Otto, A. Bilŭić, D. Babić, D. Y. Vodolazov, C. Sürgers, and C. Strunk, "Reversal of nonlocal vortex motion in the regime of strong nonequilibrium," *Phys. Rev. Lett.*, vol. 104, no. 2, 2010, doi: 10.1103/PhysRevLett.104.027005.

[33] J. Pablo-Navarro, C. Magén, and J. M. De Teresa, "Three-dimensional core-shell ferromagnetic nanowires grown by focused electron beam induced deposition," *Nanotechnology*, vol. 27, no. 28, 2016, doi: 10.1088/0957-4484/27/28/285302.

[34] K. Kohama, T. Iijima, M. Hayashida, and S. Ogawa, "Tungsten-based pillar deposition by helium ion microscope and beam-induced substrate damage," *J. Vac. Sci. Technol. B, Nanotechnol. Microelectron. Mater. Process. Meas. Phenom.*, vol. 31, no. 3, p. 031802, 2013, doi: 10.1116/1.4800983.

[35] P. Chen *et al.*, "Nanopillar growth by focused helium ion-beam-induced deposition," *Nanotechnology*, vol. 21, no. 45, 2010, doi: 10.1088/0957-4484/21/45/455302.

[36] M. Sakurai, S. Nagano, C. Joachim, and C. Joachim, "Local heat generated by a focused He+ion beam," *Nanotechnology*, vol. 31, no. 34, 2020, doi: 10.1088/1361-6528/ab91f3.

[37] C. N. Lau, N. Markovic, M. Bockrath, A. Bezryadin, and M. Tinkham, "Quantum phase slips in superconducting nanowires," *Phys. Rev. Lett.*, vol. 87, no. 21, pp. 217003-1-217003–4, 2001, doi: 10.1103/PhysRevLett.87.217003.

[38] M. Zgirski, K.-P. Riikonen, V. Touboltsev, and K. Arutyunov, "Size dependent breakdown of superconductivity in ultranarrow nanowires," *Nano Lett.*, vol. 5, no. 6, pp. 1029–1033, 2005.

[39] X. D. A. Baumans *et al.*, "Thermal and quantum depletion of superconductivity in narrow junctions created by controlled electromigration," *Nat. Commun.*, vol. 7, pp. 3–10, 2016, doi: 10.1038/ncomms10560.

[40] J. S. Lehtinen, T. Sajavaara, K. Y. Arutyunov, M. Y. Presnjakov, and A. L. Vasiliev, "Evidence of quantum phase slip effect in titanium nanowires," *Phys. Rev. B - Condens. Matter Mater. Phys.*, vol. 85, no. 9, pp. 1–7, 2012, doi: 10.1103/PhysRevB.85.094508.

[41] J. S. Lehtinen, A. Kemppinen, E. Mykkänen, M. Prunnila, and A. J. Manninen, "Superconducting MoSi nanowires," *Supercond. Sci. Technol.*, vol. 31, no. 1, 2018, doi: 10.1088/1361-6668/aa954b.

[42] G. Stan, S. B. Field, and J. M. Martinis, "Critical Field for Complete Vortex Expulsion from Narrow Superconducting Strips," *Phys. Rev. Lett.*, vol. 92, no. 9, 2004, doi: 10.1103/physrevlett.92.097003.

[43] K. K. Likharev, "Superconducting weak links," *Rev. Mod. Phys.*, vol. 51, no. 1, p. 101, 1979.